



# MobileViM: A Light-weight and Dimension-independent Vision Mamba for 3D Medical Image Analysis

Wei Dai<sup>a</sup>, Steven Wang<sup>a,\*</sup>, Jun Liu<sup>a,b,\*</sup>

<sup>a</sup>Department of Mechanical Engineering, City University of Hong Kong

<sup>b</sup>Department of Data and Systems Engineering, The University of Hong Kong

## ARTICLE INFO

### Article history:

Received -

Received in final form -

Accepted -

Available online -

**Keywords:** 3D medical imaging, Real-time segmentation, State space model, Light-weight neural network.

## ABSTRACT

Efficient evaluation of three-dimensional (3D) medical images is crucial for diagnostic and therapeutic practices in healthcare. Recent years have seen a substantial uptake in applying deep learning and computer vision to analyse and interpret medical images. Traditional approaches, such as convolutional neural networks (CNNs) and vision transformers (ViTs), face significant computational challenges, prompting the need for architectural advancements. Recent efforts have led to the introduction of novel architectures like the “Mamba” model as alternative solutions to traditional CNNs or ViTs. The Mamba model excels in the linear processing of one-dimensional data with low computational demands. However, Mamba’s potential for 3D medical image analysis remains underexplored and could face significant computational challenges as the dimension increases. This manuscript presents MobileViM, a streamlined architecture for efficient segmentation of 3D medical images. In the MobileViM network, we invent a new dimension-independent mechanism and a dual-direction traversing approach to incorporate with a vision-Mamba-based framework. MobileViM also features a cross-scale bridging technique to improve efficiency and accuracy across various medical imaging modalities. With these enhancements, MobileViM achieves segmentation speeds exceeding 90 frames per second (FPS) on a single graphics processing unit (*i.e.*, NVIDIA RTX 4090). This performance is over 24 FPS faster than the state-of-the-art deep learning models for processing 3D images with the same computational resources. In addition, experimental evaluations demonstrate that MobileViM delivers superior performance, with Dice similarity scores reaching 92.72%, 86.69%, 80.46%, and 77.43% for PENGWIN, BraTS2024, ATLAS, and Toothfairy2 datasets, respectively, which significantly surpasses existing models.

© 2025 Elsevier B. V. All rights reserved.

## 1. Introduction

The significance of early detection in medical diagnostics cannot be understated, particularly for diseases such as precancerous conditions, hepatocellular carcinoma (Quinton et al.,

2023), brain tumour (LaBella et al., 2024), and pelvic fracture (Liu et al., 2023b). These conditions often exhibit varied pathologies in terms of size, morphology, and density, posing significant challenges to detection, which is critical for improving patient outcomes. For instance, accurately identifying the inferior alveolar canal is crucial to prevent damaging the inferior alveolar nerve during maxillofacial surgeries like implant placements and molar extractions (Lumetti et al., 2024).

\*Corresponding authors: S. Wang ([steven.wang@cityu.edu.hk](mailto:steven.wang@cityu.edu.hk)) and J. Liu ([djliu@hku.hk](mailto:djliu@hku.hk)). The code is accessible through: [https://github.com/anthonyweidai/MobileViM\\_3D/](https://github.com/anthonyweidai/MobileViM_3D/).

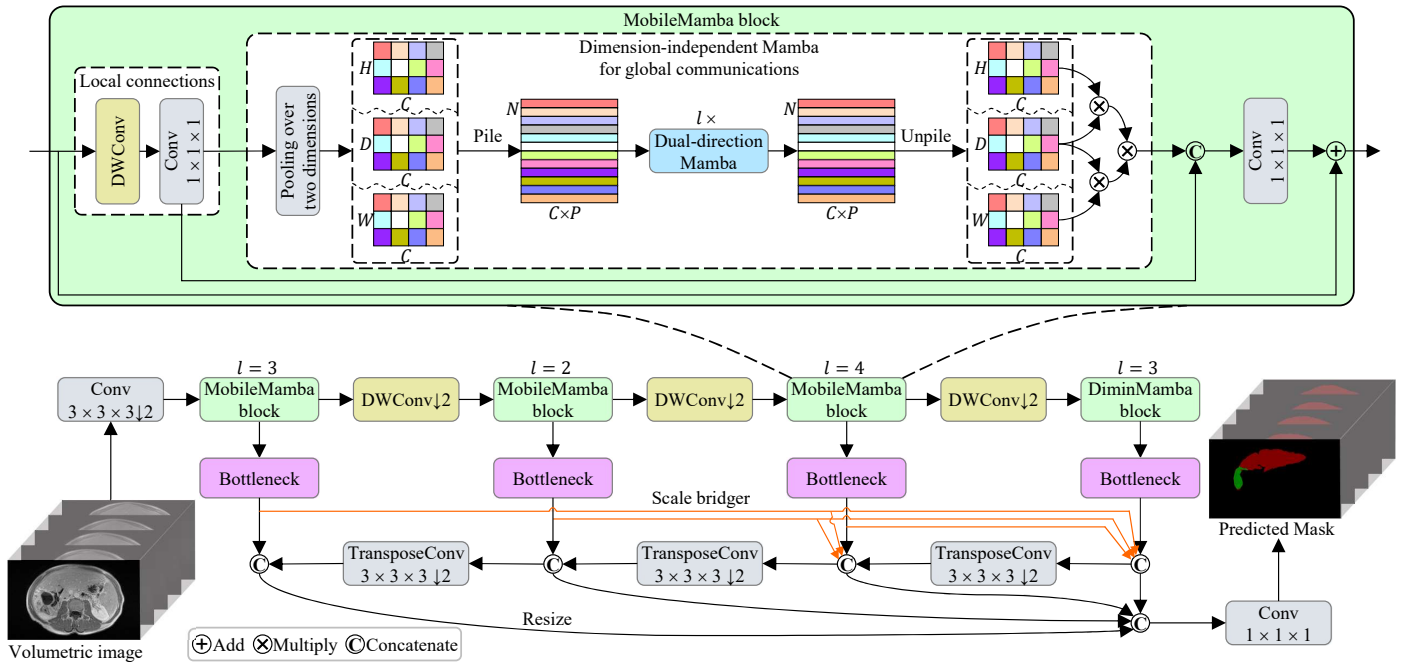


Fig. 1: Schematic of the mobile vision Mamba (MobileViM) architecture. The upper dashed box shows the MobileMamba block, combining convolutional neural networks with Mamba modules for local and global feature integration. The scale bridger, marked by the orange arrows, employs strided convolutions to reuse early features, enhancing subsequent learning stages.

Moreover, the accuracy of morphometric assessment of these pathological areas is vital for evaluating disease risk and progression (Quinton et al., 2023; Liu et al., 2023b; LaBella et al., 2024; Lumetti et al., 2024).

Advancements in deep learning have revolutionised medical image analysis, achieving diagnostic accuracies on par with human experts. However, the diversity in data from different imaging devices and patients poses significant challenges. Encoder-decoder architectures like UNet (Ronneberger et al., 2015) and its evolved versions, such as UNet++ (Zhou et al., 2019) and SwinUNETR-V2 (He et al., 2023), have demonstrated enhanced capabilities in image segmentation, essential for accurate medical analysis. Despite these advancements, there remains a pressing need for models that can operate efficiently in real-time to support clinical practices (Liu et al., 2023a; Dai et al., 2024a).

Light-weight deep learning models, optimised for speed and efficiency, are increasingly applied in clinical settings where computational resources are constrained (Dai et al., 2024a). Recent innovations in network compression (Vasu et al., 2023; Zhang and Chung, 2024) and neural architecture specification (Chen et al., 2017; Howard et al., 2019; Mehta and Rastegari, 2021; Dai et al., 2024a) have improved the computational efficiency of these models, enabling their deployment on less powerful devices, such as clinical workstations and mobile devices. While these models have been successful in general object recognition tasks, their potential in 3D medical image analysis has not been thoroughly studied.

This manuscript introduces the MobileViM architecture, specifically tailored to tackle the complexities of 3D medical image segmentation across various modalities, delivering enhanced efficiency and precision. Our key contributions include:

- **Development of MobileViM:** We present MobileViM, a novel light-weight architecture based on the vision-Mamba framework. MobileViM utilises a dimension-independent mechanism, dual-direction traversing technique, and scale bridging approach to effectively process 3D medical images at speeds over 90 frames per second (FPS) with fewer than 6.5 million parameters, setting a new benchmark for clinical applications.
- **Efficient 3D Data Processing:** The dimension-independent mechanism transforms 3D data into a more manageable 1D format, therefore reducing the parameter count by 11 million and increasing the speed of MobileViM by 70 FPS on a single graphics processing unit.
- **Bidirectional Information Flow:** The dual-direction traversing method enhances feature learning by scanning the information flow in two directions, significantly improving performance with an increase of fewer than 0.02 million parameters.
- **Multi-level Feature Extraction:** By combining Mamba and convolution strategies, MobileViM exploits local hierarchies and inter-patch relationships, facilitating an efficient analysis of medical images.
- **Cross-scale Feature Learning:** The scale bridging method mitigates compression artefacts by leveraging high-resolution early-stage features to enhance the MobileViM's ability to learn features across multiple scales.
- **Cross-dataset Validation:** MobileViM was evaluated across four public datasets (PENGWIN, BraTS2024, AT-

LAS, and ToothFairy2) and demonstrated superior performance in segmentation of various imaging modalities with a Dice similarity score exceeding 75%.

The subsequent sections will review the related literature (Sec. 2), detail the MobileViM methodology (Sec. 3), discuss experimental validations (Sec. 4), offer insights into both the strengths and potential extensions of our work (Sec. 5), and summarise our findings (Sec. 6).

## 2. Related Work

### 2.1. Medical Image Segmentation

Semantic segmentation is crucial in analysing medical images by distinguishing different tissue structures and providing granular insights. Advanced deep learning techniques have shown remarkable success, often achieving or even surpassing expert-level accuracy in medical image segmentation (Dai *et al.*, 2024b,c; Ronneberger *et al.*, 2015; Shaker *et al.*, 2024; Isensee *et al.*, 2021; Dai *et al.*, 2024d). The encoder-decoder architecture, first established by Long *et al.* (Long *et al.*, 2015), is a cornerstone in this field, consisting of an encoder for extracting features and a decoder for generating masks.

Ronneberger *et al.* (Ronneberger *et al.*, 2015) introduced a significant advancement with the UNet architecture, specifically designed for medical imaging with its U-shaped configuration. This concept was further evolved by Zhou *et al.* (Zhou *et al.*, 2019) with UNet++, which enhances multi-scale feature integration, and by Isensee *et al.* (Isensee *et al.*, 2021), who modified UNet to accommodate both 2D and 3D imaging contexts with nnUNet. He *et al.* (He *et al.*, 2023) integrated Swin Transformer to develop SwinUNETR-V2, aimed at multi-organ CT and MRI analyses. Shaker *et al.* (Shaker *et al.*, 2024) developed UNetR++, which incorporates attention mechanisms to improve the extraction of spatial features. Chen *et al.* (Chen *et al.*, 2024) introduced TransUNet, which combines vision transformers and CNNs to better capture long-range dependencies within images and refine predicted regions. Despite the success of these models, their comparatively large size and computational demands often limit their use in real-time medical applications.

### 2.2. State Space Model

Structured state space models (SSMs) address computational inefficiencies associated with processing long sequences in transformers. The structured state space sequence (S4) models, developed by Gu *et al.* (Gu *et al.*, 2022), present a viable alternative to traditional transformers, demonstrating linear or near-linear scaling with sequence length. Traditional S4 models, however, face challenges in capturing contextual nuances within information-dense data such as text and images (Gu *et al.*, 2022). To overcome these limitations, Gu *et al.* (Gu and Dao, 2024) have enhanced S4 models by introducing advanced selection mechanisms and a recurrence scan strategy, known as Mamba. The Mamba model integrates sequence length information more effectively into SSMs, thereby improving content-based reasoning. Dao *et al.* (Dao and Gu, 2024) introduced

Mamba2, an advancement of the original Mamba model that integrates SSMs with various attention mechanisms through semi-separable matrix transformations and incorporates a parallel training framework for improved efficiency.

In visual tasks, Zhu *et al.* (Zhu *et al.*, 2024) modified 2D image into a format suitable for the 1D capabilities of the SSM and adapted the Mamba model for bidirectional processing, which enhances image classification and segmentation performance while reducing computational expenses compared to ViTs. Besides, Liu *et al.* (Liu *et al.*, 2024b) enhanced the standard SSMs by applying a raster scan over 2D images using four different paths, developing VMamba, which addresses SSMs' limitation to only process 1D data. Zhu *et al.* (Zhu *et al.*, 2025) advanced VMamba by incorporating context clusters to learn local features. Furthermore, Ruan *et al.* (Ruan and Xiang, 2024) improved the UNet architecture by incorporating the Mamba module, creating VMUNet, which offers broader modeling capabilities. Additionally, Xing *et al.* (Xing *et al.*, 2024) implemented Mamba blocks within the encoder portion of UNet, termed SegMamba, specifically for handling volumetric features in 3D colorectal cancer imaging. Moreover, Liu *et al.* (Liu *et al.*, 2024a) investigated the advantages of using pretrained weights from ImageNet to boost medical image segmentation performance. Despite these advancements, a general oversight remains regarding the computational costs incurred during the testing phase, which is crucial for real-time disease diagnosis.

### 2.3. Light-weight Neural Networks

#### 2.3.1. Network Compression

Network compression integrates strategies that impose structural constraints either during or after the training process to reduce redundancy in the network. Techniques include direct compression during training (Zhang and Chung, 2024) or applying compression after learning is complete (Vasu *et al.*, 2023). One notable method within network compression is knowledge distillation, which involves transferring features from a larger "teacher" network to a smaller "student" network during training. While knowledge distillation reduces the parameter count needed during inference, it introduces the computational burden of managing and training two separate networks (Zhang and Chung, 2024). Another method used in network compression is network reparameterisation, which trains the network using adaptable modules and deploys a streamlined version for inference. Like knowledge distillation, network reparameterisation increases training complexity due to the adjustable nature of the modules involved (Vasu *et al.*, 2023).

#### 2.3.2. Neural Architecture Design

Designing architectures that are mobile-friendly provides more flexibility than network compression alone. A key strategy in developing light-weight CNNs involves the use of depthwise separable convolutions, which replace standard convolutions with depthwise and pointwise layers to significantly cut the computational costs while preserving performance (Howard *et al.*, 2019; Mehta and Rastegari, 2021; Dai *et al.*, 2024a). Another powerful method is the use of dilated convolutions, especially in conjunction with atrous spatial pyramid pooling

(ASPP) (Chen *et al.*, 2017), which employs dilated convolutions to capture spatial features at varying scales, improving the delineation of segmentation boundaries. For ViTs suited to mobile environments, the MobileViT architecture has been developed, merging convolutional layers with transformer components in a hybrid block to address latency from image splitting and to maintain inductive biases (Mehta and Rastegari, 2021; Dai *et al.*, 2024a). Lee *et al.* (Lee *et al.*, 2023) have integrated large-kernel and depthwise separable CNNs with swin transformer blocks in their 3DUX-Net, reducing the number of normalisation and activation layers and thereby minimising the model’s parameters.

In the realm of efficient Mamba architecture, Pei *et al.* (Pei *et al.*, 2024) developed an atrous-based scanning approach to optimise patch sampling and reduce the complexity of vision Mamba. Yao *et al.* (Yao *et al.*, 2024) have worked on enhancing content-awareness representations and encoding semantic relationships by reducing spectral variability and confusion in hyperspectral imaging through the integration of SSMS. Furthermore, quantisation of state variances within the Mamba has been implemented, storing state caches as low-bit elements for low-rank approximation (Anonymous, 2024). Additionally, Lee *et al.* (Lee *et al.*, 2024) streamlined the sequence length of hidden states in Mamba to lower computational costs.

Although these mobile architectures achieve performance comparable to conventional networks, their potential in medical image analysis, particularly in 3D imaging, has not been adequately addressed. We propose a light-weight vision Mamba architecture that incorporates the dimension-independent mechanism, dual-direction process technique, and the scale bridge, capable of conducting segmentation tasks on 3D medical images and overcoming current limitations in the field.

### 3. Methodology

#### 3.1. Overall Framework

This section introduces the mobile vision Mamba (MobileViM) network, as illustrated in Fig. 1. The network comprises two main elements: the MobileMamba block and the scale bridge.

**MobileMamba Block:** As highlighted by the green dashed box in Fig. 1, the MobileMamba block is structured into sections for global communications and local connections. The block features the **dimension-independent** (Dimin) mechanism, which is designed to capture a broader range of spatial hierarchies, essential for advanced contextual feature learning. The Dimin Mamba employs a dimension-independent mechanism that processes each dimension of 3D data individually, thereby significantly boosting computational efficiency. Moreover, the MobileMamba block uses a bidirectional information flow to process stacked patches in onwads and backwards directions, termed the **dual-direction Mamba**. The dual-direction traversal of patches ensures comprehensive integration of spatial information, enhancing the block’s capability in feature extraction.

Before the Mamba module, the depthwise separable convolution (a depthwise convolution and a pointwise convolution)

Table 1: Configuration variants of the MobileViM encoders. This table details the variations in the input and output channels for the Conv3 × 3 × 3 ↓ 2, DWConv ↓ 2, and MobileMamba blocks across two different model scales.

Layer	Output size	Output channels	
		XS	S
Conv3 × 3 × 3 ↓ 2	64×64×64	32	32
MobileMamba block	64×64×64	48	48
DWConv ↓ 2	32×32×32	48	64
MobileMamba block	32×32×32	72	96
DWConv ↓ 2	16×16×16	64	96
MobileMamba block	16×16×16	96	144
DWConv ↓ 2	8×8×8	80	128
MobileMamba block	8×8×8	120	192

with relatively small kernel size, 1 × 1 × 1 or 3 × 3 × 3, is applied to learn the local connections of voxels. After the Mamba module, the feature concatenation and addition are employed to improve the local and global fusion of features that come from the output of convolutions or Mambas.

**Scale Bridge:** This component consists of a series of strided convolutions within the feature map, as depicted by the orange arrows in Fig. 1. It facilitates the tracking of feature evolution throughout the learning process, guiding the network’s subsequent stages.

**Other Components:** The architecture initiates with an encoder, structured as shown in the first row of blocks in Fig. 1. It starts with a Conv3 × 3 × 3 ↓ 2, followed by four MobileMamba blocks and three DWConv ↓ 2. This setup optimises traditional encoders by utilising fewer strided convolutions — only four in total — to achieve a more compact model size and faster inference speeds. Within the architecture, each “Bottleneck” module integrates a sequence of convolutions: starting with a 3 × 3 × 3 convolution, followed by a 1 × 1 × 1 convolution to compress the feature space, and another 1 × 1 × 1 convolution for feature refinement. “DWConv”, or depthwise convolution, is utilised throughout the network to decrease computational load while maintaining robust feature extraction capabilities.

In this study, the model is scaled into two sizes to meet varying computational and performance criteria: “extra small” and “small”. Each scale, detailed in Tab. 1, incorporates specific architectural adjustments to effectively balance the constraints of model size with the desired performance objectives.

#### 3.2. State Space Model Foundations

Structured state space sequence (S4) models, a specialised subset of state space models (SSMs), are designed to emulate continuous systems by mapping one-dimension sequences  $x(t) \in \mathbb{R}^M$  to  $y(t) \in \mathbb{R}^M$  through implicit states  $h(t) \in \mathbb{R}^{(M,1)}$ . S4 models are characterized by four parameters: timescale parameter  $\Delta$ , evolution parameter  $A$ , and projection parameters  $B$  and  $C$ , which define the sequence-to-sequence transformation (Gu *et al.*, 2022). The output  $y(t)$  of continous system are defined as:

$$\begin{aligned} \frac{dh(t)}{dt} &= Ah(t) + Bx(t) \\ y(t) &= C^T h(t) \end{aligned} \quad (1)$$

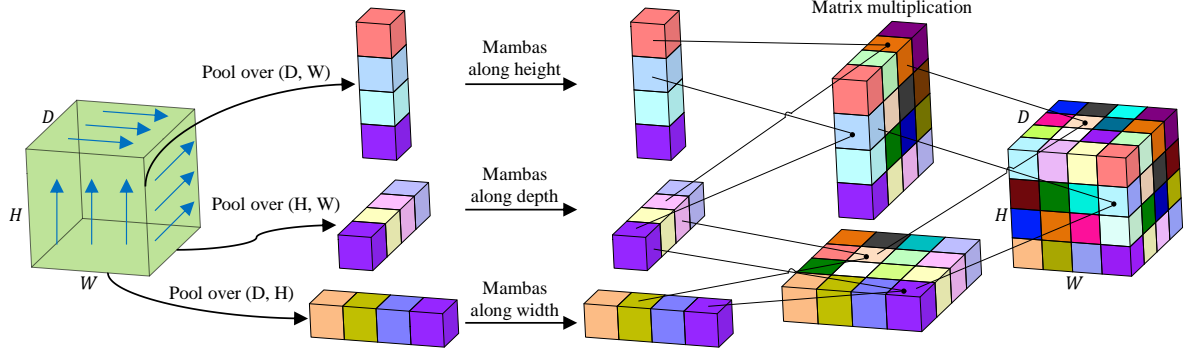


Fig. 2: Depiction of the dimension-independent (Dimin) mechanism. Matrix multiplication ensures that each voxel incorporates comprehensive information from all three dimensions.

where  $M$  is the state expansion factor,  $\mathbf{A} \in \mathbb{R}^{(M,M)}$ ,  $\mathbf{B}, \mathbf{C} \in \mathbb{R}^{(M,1)}$ .

S4 models discretizes continuous parameters  $\mathbf{A}$  and  $\mathbf{B}$  and transform them into discrete parameters  $\bar{\mathbf{A}}$  and  $\bar{\mathbf{B}}$  by using a time step  $\Delta$  and the zero-order hold method:

$$\begin{aligned} \bar{\mathbf{A}} &= \exp(\Delta \mathbf{A}) \\ \bar{\mathbf{B}} &= (\Delta \mathbf{A})^{-1} (\exp(\Delta \mathbf{A}) - \mathbf{I}) \cdot \Delta \mathbf{B} \end{aligned} \quad (2)$$

where  $\mathbf{I}$  denotes the identity matrix.

Using Eq. (1) and Eq. (2), the discrete system can be formulated as:

$$\begin{aligned} \mathbf{h}_t &= \bar{\mathbf{A}} \mathbf{h}_{t-1} + \bar{\mathbf{B}} \mathbf{x}_t \\ \mathbf{y}_t &= \mathbf{C}^\top \mathbf{h}_t \end{aligned} \quad (3)$$

Finally, S4 models compute results through a global convolution:

$$\begin{aligned} \bar{\mathbf{K}} &= (\bar{\mathbf{C}} \bar{\mathbf{B}}, \bar{\mathbf{C}} \bar{\mathbf{A}} \bar{\mathbf{B}}, \dots, \bar{\mathbf{C}} \bar{\mathbf{A}}^k \bar{\mathbf{B}}, \dots) \\ \mathbf{y} &= \mathbf{x} * \bar{\mathbf{K}} \end{aligned} \quad (4)$$

where  $\bar{\mathbf{K}} \in \mathbb{R}^N$  is a structured convolutional kernel, and  $*$  represents the convolution operation.  $k \in [1, N-1]$  is the kernel size and  $N$  denotes the length of the input sequence.

Mamba extends the S4 models by adapting the changes in tensor shapes according to parameters, thereby enabling the learning of the long-range features from text or images (Dao and Gu, 2024). If the parameters ( $\mathbf{A}, \mathbf{B}, \mathbf{C}$ ) can vary in time, the S4 model can selectively choose to focus on or ignore inputs at every timestep. Then the Eq. (3) can be enhanced and presented by:

$$\begin{aligned} \mathbf{h}_t &= \bar{\mathbf{A}}_t \mathbf{h}_{t-1} + \bar{\mathbf{B}}_t \mathbf{x}_t \\ \mathbf{y}_t &= \mathbf{C}_t^\top \mathbf{h}_t \end{aligned} \quad (5)$$

where  $\mathbf{h}_t \in \mathbb{R}^{M,N}$ ,  $\mathbf{A}_t \in \mathbb{R}^M$ , and  $\Delta_t, \mathbf{B}_t, \mathbf{C}_t \in \mathbb{R}^{M,N}$ .

### 3.3. Dimension-independent Mechanism

In our research, we have extended the application of the Mamba model, originally developed for analysing 1D sequential data, to accommodate higher-dimensional data, particularly images. To achieve this, we reformat the input data, represented as a tensor  $\mathbf{X} \in \mathbb{R}^{C \times D \times H \times W}$ , into a series of 2D patches  $\mathbf{X}_p \in \mathbb{R}^{N \times (C \times P)}$ . Here,  $C$  denotes the number of channels, and the tuple  $(D, H, W)$  specifies the dimensions of the input tensor.

The variable  $N$  indicates the total number of patches and concurrently serves as the length of the input, while  $P$  represents the patch size.

Driven by the goal of reducing computational demands and enhancing efficiency, we pose the question: *Is it possible to "linearise" data dimensions without loss of information?* Previous research has explored separating feature maps along dimensions, using attention maps as a skip connection to re-weight features on the main flow (Hou et al., 2021). However, directly separating the dimensions of main flow feature maps can result in losing information necessary for effective feature learning.

To address this, we have implemented a straightforward but effective matrix multiplication using single-dimension patches from the decomposition of the Mamba outputs. In the tested 3D image datasets, although the height and width dimensions are consistent, the depth dimension varies. Consequently, matrix multiplication is applied separately for both height and width to the depth dimension. This feature fusion approach via matrix multiplication ensures that each voxel has information from three dimensions, reintegrating the separate dimensions. We refer to this method as the **dimension-independent (Dimin) mechanism**. Dimin can be considered a context-learning operation that significantly enhances global communications among voxels. As demonstrated in the ablation study detailed in Sec. 4.3, the Dimin mechanism improves model performance with reduced computational load. The Dimin mechanism is illustrated in Fig. 1 and detailed in Fig. 2.

The SSM in the Mamba module and the self-attention mechanism in the ViT are pivotal for adaptively providing a global context. Considering a visual sequence represented by  $\mathbf{X}_p \in \mathbb{R}^{N \times E}$ , the computational complexities of self-attention and SSM differ significantly:

- The computational complexity of self-attention scales quadratically with the sequence length  $N$ :

$$\Omega(\text{self-attention}) = 4NE^2 + 2N^2E \quad (6)$$

- In contrast, the complexity for SSM scales linearly with

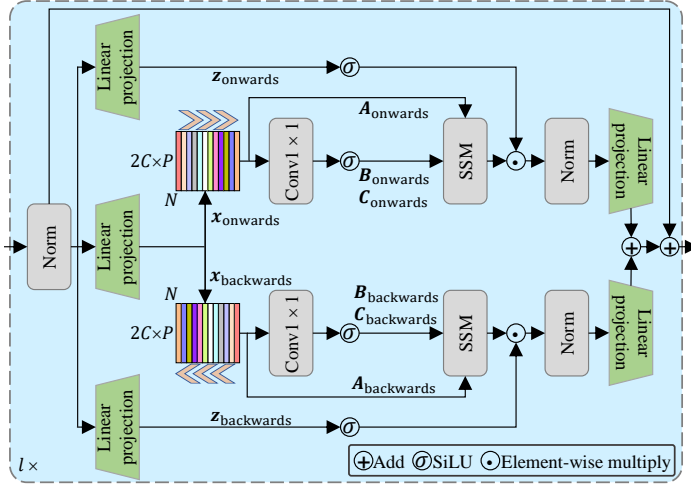


Fig. 3: Diagram of the dual-direction Mamba module. This module applies a bidirectional traversing technique to thoroughly process data and effectively capture patch information.

the sequence length  $N$ :

$$\begin{aligned}\Omega(\text{SSM}) &= 3N(2E)M + N(2E)M, \\ &= 8NEM\end{aligned}\quad (7)$$

where  $M$  is a constant parameter of state size, typically set to 16.  $E$  denotes the size of the input sequence.

With the dimension-independent mechanism, the computational complexity for the Dimin framework can be significantly reduced by adjusting the sequence length to the **cube root** of  $N$ . Assuming equal dimensions  $D$ ,  $H$ , and  $W$ , the computational complexity can be expressed as:

$$\begin{aligned}\Omega(\text{Dimin}) &= 3(3N^{1/3}(2E)M + N^{1/3}(2E)M) \\ &= 24N^{1/3}EM\end{aligned}\quad (8)$$

Reducing computational complexity is crucial for the Dimin framework to manage applications involving gigapixel images with extensive sequence lengths effectively.

### 3.4. Dual-direction Information Flow

Inspired by the foundational concepts in the Mamba2 block (Dao and Gu, 2024) and the bidirectional sequence mixer (Hwang *et al.*, 2024), we propose an advanced dual-direction Mamba block tailored for vision processing tasks. This new block, depicted as the blue block of Fig. 1 and elaborately described in Fig. 3, is further outlined algorithmically in Algorithm 1. The dual-direction vision mamba utilises  $l$  blocks to process patches, learning representations among patches to enhance its analytical capabilities.

The parameter  $A$  is initialised using a continuous uniform distribution over the interval  $[1, M]$ . Each input patch  $\{X_p\}_i$  undergoes normalisation before being divided into two pathways  $x$  and  $z$ , each expanded by a factor of 2.

Bidirectional scanning refers to the process where  $x$  pathway is analysed along the length dimension  $N$  in two opposite directions — onwards and backwards. This results in two vectors:

### Algorithm 1 Pseudocode: Dual-direction Mamba.

---

**Require:**  $\{X_p\}_i : (\mathbf{B}, \mathbf{N}, \mathbf{E})$   
**Ensure:**  $\{X_p\}_{i+1} : (\mathbf{B}, \mathbf{N}, \mathbf{E})$

# Normalize the input patch  $\{X_p\}_i$   
 $\{X_p\}'_i : (\mathbf{B}, \mathbf{N}, \mathbf{E}) \leftarrow \text{Norm}(\{X_p\}_i)$   
 $x : (\mathbf{B}, \mathbf{N}, 2\mathbf{E}) \leftarrow \text{Linear}^x(\{X_p\}'_i)$   
 # Process data in opposite directions  
**for**  $d$  in {onwards, backwards} **do**  
    $x'_d : (\mathbf{B}, \mathbf{N}, 2\mathbf{E}) \leftarrow \text{SiLU}(\text{Conv1d}_d(x_d))$   
    $B_d : (\mathbf{B}, \mathbf{N}, \mathbf{M}) \leftarrow \text{Linear}^B(x'_d)$   
    $C_d : (\mathbf{B}, \mathbf{N}, \mathbf{M}) \leftarrow \text{Linear}^C(x'_d)$   
   # Generate value from continuous uniform distribution  
    $A_d : (\mathbf{M}) \leftarrow U(1, M)$   
   # Compute bias-adjusted Softplus for positive  $\Delta_d$   
    $\Delta_d : (\mathbf{B}, \mathbf{N}, 2\mathbf{E}) \leftarrow \log(1 + \exp(\text{Linear}^A(x'_d) + b_d^A))$   
    $\bar{A}_d : (\mathbf{B}, \mathbf{N}, 2\mathbf{E}, \mathbf{M}) \leftarrow \Delta_d \otimes A_d$   
    $\bar{B}_d : (\mathbf{B}, \mathbf{N}, 2\mathbf{E}, \mathbf{M}) \leftarrow \Delta_d \otimes B_d$   
   # Initialize state  $h_d$  and output  $y_d$  to 0  
    $h_d : (\mathbf{B}, 2\mathbf{E}, \mathbf{M}) \leftarrow \text{zeros}(\mathbf{B}, 2\mathbf{E}, \mathbf{M})$   
    $y_d : (\mathbf{B}, \mathbf{N}, 2\mathbf{E}) \leftarrow \text{zeros}(\mathbf{B}, \mathbf{N}, 2\mathbf{E})$   
   # State-space model iterations  
   **for**  $i$  in  $\{0, \dots, N-1\}$  **do**  
      $h_d = \bar{A}_d[:, i, :, :] \odot h_d + \bar{B}_d[:, i, :, :] \odot x'_d[:, i, :, \text{None}]$   
      $y_d[:, i, :] = h_d \otimes C_d[:, i, :]$   
   **end for**  
   # Apply gating to the outputs  $y_d$   
    $z_d : (\mathbf{B}, \mathbf{N}, 2\mathbf{E}) \leftarrow \text{Linear}^{z_d}(\{X_p\}'_i)$   
    $y'_d : (\mathbf{B}, \mathbf{N}, \mathbf{E}) \leftarrow \text{Linear}^T(\text{Norm}(y_d \odot z_d))$   
**end for**  
 # Combine results with a shortcut connection  
 $\{X_p\}_{i+1} : (\mathbf{B}, \mathbf{N}, \mathbf{E}) \leftarrow (y'_{\text{onwards}} + y'_{\text{backwards}}) + \{X_p\}_i$   
 Return:  $\{X_p\}_{i+1}$

---

$x_{\text{onwards}}$  and  $x_{\text{backwards}}$ . Each directional output, denoted as  $x_d$  where  $d$  can be either 'onwards' or 'backwards', is projected into its respective matrices  $B_d$ ,  $C_d$ , and  $\Delta_d$ . The values in  $\Delta_d$  is then used to discretize the parameters  $A_d$  and  $B_d$ , converting them to  $\bar{A}_d$  and  $\bar{B}_d$ , respectively.

The processed outputs from the SSM recurrences, denoted as  $y_d$ , are then controlled by the gating functions linked to  $z_d$ . After gating, the outputs are normalised and aggregated to produce the enhanced patch  $\{X_p\}_{i+1}$ . The default setting for the SSM's state expansion factor,  $M$ , is configured to 16.

This dual-direction approach amplifies the depth of data analysis and significantly boosts the model's precision in handling and interpreting complex visual information within bidirectional contexts.

### 3.5. Mobile Vision Mamba

To improve local and contextual representation learning while maintaining relatively low computational demands, we developed the MobileMamba block by applying the Dimin mechanism (Sec. 3.3), dual-direction Mamba (Sec. 3.4), and convolution techniques, which is visualised as the green boxes in Fig. 1. The MobileMamba block combines depthwise separable convolutions, followed by Mamba operations using the

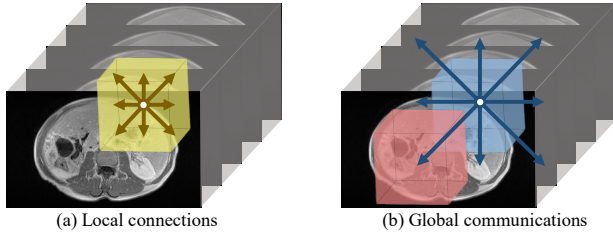


Fig. 4: Interactions within the MobileMamba block. Convolutions detect connections among local features, while Mamba elements establish long-range spatial communications.

Dimin mechanism with dual-direction information flow, and concludes with a subsequent convolutional layer. The configuration includes  $l$  dual-direction Mamba blocks within the Dimin Mamba framework.

The MobileMamba block bridges the operational disparities between conventional convolution techniques and the novel Mamba methodologies by alternating between piled and unpiled feature maps. This approach mitigates the intrinsic limitations of Mamba blocks, such as their absence of inherent biases and their considerable reliance on large volumes of training data (Gu and Dao, 2024).

Within the MobileMamba block, convolutional operations are meticulously optimised to extract precise local features from medical images, including but not limited to angles, corners, edges, and colour variations. As visualised in Fig. 4a, this process ensures the analysis of local features before processing global information. The subsequent Dimin Mamba framework is tailored to assimilate broader attributes encompassing morphology, intensity variations, the general colour distribution of medical entities, and their spatial interrelations, as shown in Fig. 4b. The Dimin Mamba module captures long-range spatial dependencies among encoded image patches. The efficacy of this approach is supported by the results from the ablation study, outlined in Tab. 4, which demonstrate that the Dimin Mamba module significantly enhances the segmentation capabilities of the MobileViM model.

### 3.6. Scale Bridger

The performance of neural networks in processing medical images often diminishes as feature map shapes become more compressed, mainly due to the introduction of compression artifacts (Dai et al., 2024b). To address this challenge, our study introduces a scale bridger module that leverages higher-resolution features from earlier stages within the network. Assuming that  $o$  denotes the target encoder stage, the output at this stage,  $y_o$ , is calculated using the formula:

$$y_o = \sum_{s=1}^{o-1} g(x_s, o) \quad (9)$$

where  $x_s$  refers to the input tensor at encoder stage  $s$ , and  $o - s$  indicates the number of the strided convolutions between stage  $s$  and  $o$ . The function  $g(x_s, o)$  represents the application of  $(o - s)$  sets of strided convolutions, facilitating the integration of features across different scales.

As depicted by orange arrows in Fig. 1, this cross-scale integration method, described by Eq. (9), plays a crucial role in enhancing the model's capability to preserve higher-resolution information through the network stages. This approach mitigates the loss of detail due to compression and improves the model's overall accuracy of the model in medical image analysis.

### 3.7. Loss Function

To evaluate the accuracy of the predicted segmentation mask against the ground truth in medical image segmentation tasks, we employed both cross-entropy and Dice losses, which are effective for voxel-level classification. The efficacy of combining these two losses has been well-documented in medical imaging research, as outlined by (Milletari et al., 2016).

The cross-entropy loss, which assesses the discrepancy between predicted probabilities and actual labels, is defined as:

$$\mathcal{L}_{CE} = -\frac{1}{T} \sum_{k=1}^T \sum_{c=1}^Q y_{k,c} \log_2(p_{k,c}) \quad (10)$$

where  $T$  denotes the total number of input images,  $Q$  denotes the number of classes,  $y_{k,c}$  is the binary indicator for class membership, and  $p_{k,c}$  is the predicted probability that the  $k^{\text{th}}$  voxel belongs to the  $c^{\text{th}}$  class.

The Dice loss, aimed at quantifying the similarity between the predicted and actual segmentations, is mathematically expressed as:

$$\mathcal{L}_{Dice} = -\frac{2}{Q} \sum_{c=1}^Q \frac{\sum_{k=1}^T p_{k,c} y_{k,c}}{\sum_{k=1}^T p_{k,c} + \sum_{k=1}^T y_{k,c}} \quad (11)$$

To compute the total segmentation loss, we sum the Dice and cross-entropy losses:

$$\mathcal{L}_{total} = \mathcal{L}_{CE} + \mathcal{L}_{Dice} \quad (12)$$

## 4. Experimental Results

### 4.1. Evaluation Protocol

#### 4.1.1. Dataset

In this study, we assessed the effectiveness of MobileViMs and compared it with seven other leading-edge models using four benchmark datasets: PENGWIN (Liu et al., 2023b), BraTS2024 (LaBella et al., 2024), ATLAS (Quinton et al., 2023), and ToothFairy2 (Lumetti et al., 2024).

**PENGWIN Dataset:** This dataset includes 100 pelvic computer tomography (CT) scans that prominently feature sacrum and hipbone fragments, enabling detailed analysis of pelvic structures.

**BraTS2024 Dataset:** With 500 post-contrast MRI scans of the brain, this dataset is the third task of BraTS2024 challenges and is tailored for the automated segmentation of meningioma gross tumour volumes, offering extensive data for brain tumour analysis.

Table 2: Segmentation performance across different models on PENGWIN, BraTS2024, ATLAS, and ToothFairy2 datasets. The best results are highlighted in **bold**, and the second-best results are underlined.

Methods	Computational efficiency			Dice/%				RMSE			
	# Params /million	MACs /billion	Speed /FPS $\uparrow$	PENGWIN	BraTS2024	ATLAS	ToothFairy2	PENGWIN	BraTS2024	ATLAS	ToothFairy2
UNet++ (Zhou et al., 2019)	31.64	8045.55	8	83.53	76.90	78.05	<b>79.30</b>	$1.21 \times 10^{-1}$	$2.65 \times 10^{-2}$	$1.61 \times 10^{-1}$	<b>1.79</b>
SegMamba (Xing et al., 2024)	66.86	6214.21	9	90.89	79.66	77.13	76.44	<b><math>1.13 \times 10^{-1}</math></b>	$2.58 \times 10^{-2}$	$1.72 \times 10^{-1}$	<u>1.87</u>
3DUX-Net (Lee et al., 2023)	53.01	5988.81	9	79.02	85.62	78.19	76.00	$1.51 \times 10^{-1}$	<b><math>2.14 \times 10^{-2}</math></b>	$1.58 \times 10^{-1}$	1.91
SwinUNETR-V2 (He et al., 2023)	15.70	798.91	13	89.60	85.03	78.37	73.18	$1.30 \times 10^{-1}$	$2.45 \times 10^{-2}$	$1.64 \times 10^{-1}$	2.00
nnUNet (Isensee et al., 2021)	31.17	2966.87	23	<b>93.05</b>	86.01	79.39	76.71	<b><math>1.13 \times 10^{-1}</math></b>	<u><math>2.31 \times 10^{-2}</math></u>	<u><math>1.53 \times 10^{-1}</math></u>	1.94
TransUNet (Chen et al., 2024)	109.34	1956.79	36	81.43	84.42	76.80	64.78	$1.56 \times 10^{-1}$	$2.61 \times 10^{-2}$	$1.65 \times 10^{-1}$	2.04
UNetR++ (Shaker et al., 2024)	42.97	550.91	67	89.53	84.97	78.47	64.58	$1.40 \times 10^{-1}$	$2.43 \times 10^{-2}$	$1.59 \times 10^{-1}$	2.17
<b>MobileViM<sub>s</sub> (ours)</b>	<u>6.29</u>	<u>195.56</u>	<u>91</u>	<u>92.72</u>	<b>86.69</b>	<b>80.46</b>	<u>77.43</u>	$1.30 \times 10^{-1}$	$2.42 \times 10^{-2}$	<b><math>1.52 \times 10^{-1}</math></b>	2.05
<b>MobileViM<sub>xs</sub> (ours)</b>	<b>2.89</b>	<b>131.55</b>	<b>94</b>	89.97	<u>86.18</u>	<u>79.65</u>	75.54	$1.42 \times 10^{-1}$	$2.44 \times 10^{-2}$	$1.60 \times 10^{-1}$	2.07

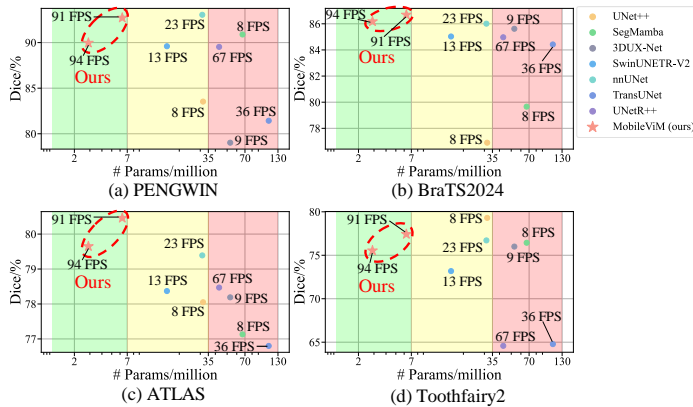


Fig. 5: Comparison of MobileViMs and SOTA models on segmentation Dice similarity scores, # Params, and inference speed.

**ATLAS Dataset:** Comprising 90 T1 contrast-enhanced magnetic resonance imaging (CE-MRI) scans, this dataset is focused on liver tumours. It provides a basis for evaluating organ-specific tumour detection and segmentation capabilities.

**ToothFairy2 Dataset:** This collection consists of 480 cone beam computer tomography (CB-CT) scans, divided into 43 different classes representing various anatomical features and dental structures, including the jaws, maxillary sinus, pharynx, and dental restorations like bridges, crowns, and implants.

For a thorough and rigorous evaluation, all datasets were partitioned into training and testing subsets with a ratio of 4:1. This setup ensures that our model’s performance is measured accurately across different medical imaging modalities and anatomical challenges.

#### 4.1.2. Implementation Details

This research utilised an AMD Ryzen 9 7950X CPU and an NVIDIA RTX 4090 GPU to conduct experiments. We trained the segmentation models using Dice and cross-entropy loss functions, and optimisation was carried out with the AdamW optimiser (Loshchilov and Hutter, 2017). The models were trained with a mini-batch size of four. We employed several data augmentation techniques to enhance model robustness, including sampling foreground and background patches and ap-

plying random transformations consisting of rotating and flipping. The initial learning rate was set to  $1.6 \times 10^{-6}$ , which decayed to  $1.6 \times 10^{-7}$ , throughout 100 epochs, following a cosine annealing schedule (Loshchilov, Ilya and Hutter, Frank, 2016). To ensure reliability, results were averaged over three separate training and testing cycles. All models were evaluated under these standardised conditions. For the models in the control group, any unspecified configurations adhered to their respective official implementations. The experimental code was implemented using the PyTorch (Paszke et al., 2019) framework.

#### 4.1.3. Evaluation Metric

To comprehensively assess the semantic segmentation performance of the models under study, we employed a variety of metrics. The complexity of each model was gauged by the number of parameters, denoted as # Params and expressed in millions. Additionally, we quantified the computational demand of each model using multiply-accumulate operations (MACs), reported in billions, and evaluated real-world usability by measuring inference speed in frames per second (FPS). For a precise assessment of voxel-level accuracy, we utilised the mean Dice similarity coefficient (Dice), crucial for evaluating the segmentation precision in medical imaging contexts. Furthermore, the root mean square error (RMSE) was employed to evaluate the discrepancies between the predicted volumes and the ground truth. These metrics together provide a detailed evaluation framework, enabling the measurement of segmentation accuracy and effectiveness across different imaging applications.

#### 4.2. Results for Medical Image Segmentation

To assess the efficacy of MobileViMs in processing 3D data, we conducted a comparative study with seven state-of-the-art (SOTA) networks using the PENGWIN, BraTS2024, ATLAS, and ToothFairy2 datasets. The results of this investigation are visualised in Fig. 5 and detailed in Tab. 2. For analytical purposes, the models were classified based on their parameter count into three categories: “small” for models with fewer than 7 million parameters, “medium” for those with 7 – 35 million parameters, and “large” for those exceeding 35 million parameters.



As indicated in Fig. 5, MobileViMs are positioned in the top-left region, demonstrating superior performance relative to other SOTA models with a comparatively minimal parameter count. For instance, MobileViM<sub>s</sub> utilised only 6.29 million parameters and 195.56 billion MACs, but it recorded the highest Dice scores of 86.69% and 80.46% for the BraTS2024 and ATLAS datasets, respectively. MobileViM<sub>s</sub> also achieved the second-highest Dice scores of 92.72% and 77.43% for the PENGWIN and ToothFairy2 datasets, respectively. Moreover, MobileViM<sub>s</sub> outperformed SegMamba, which also features Mamba modules, by more than 1.83%, +7.03%, +3.33%, and +0.99% in Dice scores across the four datasets, respectively.

Despite nnUNet and UNet++ obtaining the highest Dice scores of 93.05% and 79.30% in the PENGWIN and ToothFairy2 datasets, respectively, their performance was limited by lower frame rates (<25 FPS) and higher parameter count (>31 million), reflecting significant resource consumption. According to Tab. 2, the inference speeds of MobileViMs are over 90 FPS, more than 20 FPS faster than other SOTA models. Given their high speeds, MobileViMs are suitable for clinical diagnostics involving 3D medical imaging, such as CT and MRI scans. In contrast, models like UNet++, Segmamba, 3DUX-Net, SwinUNETR-V2, and nnUNet consume over 790 billion MACs and operate below 25 FPS in recognising 3D images, as illustrated in the yellow or red regions of Fig. 5.

Furthermore, the smallest model, MobileViM<sub>xs</sub>, with only 2.89 million parameters, managed to secure the second-best Dice scores of 86.18% in the BraTS2024 dataset for brain tumours and 79.65% in the ATLAS dataset for liver cancers, with a rapid inference speed of 94 FPS. The aforementioned results emphasise the efficacy and adaptability of MobileViMs in processing and diagnosing 3D medical images across diverse medical domains.

Further analysis detailed in Tab. 2 reveals that MobileViM<sub>s</sub> achieved the lowest RMSE of  $1.52 \times 10^{-1}$  in the ATLAS dataset and the third-lowest RMSE of  $2.42 \times 10^{-2}$  in the BraTS2024 dataset. MobileViM<sub>s</sub> also obtained competitive RMSE of  $1.30 \times 10^{-1}$  and 2.05 in the PENGWIN and ToothFairy2 datasets, respectively, only 15% higher than the top-performing models in these respective datasets. Moreover, the smallest model, MobileViM<sub>xs</sub> recorded RMSE of  $1.42 \times 10^{-1}$ ,  $2.44 \times 10^{-2}$ ,  $1.60 \times 10^{-1}$ , and 2.07 in the PENGWIN, BraTS2024, ATLAS, and ToothFairy2 datasets respectively. These results highlight the capability of MobileViMs to delineate regions of interest in 3D medical images with significantly low error rates.

To further analyse the model's performance across different classes within the datasets, we focus on the results in the PENGWIN dataset. As illustrated in Tab. 3, MobileViM<sub>s</sub> outperformed other SOTA methods in specific anatomical areas, achieving Dice scores of 92.15% for left hipbones and 92.18% for right hipbones. In addition, MobileViM<sub>s</sub> recorded a Dice score of 86.76% in identifying sacrums, which is -6.80% lower than the best results achieved by UNet++. Furthermore, all evaluated methods consistently delivered Dice scores over 99.70% in distinguishing the background in CT scans of pelvic fractures.

To visualise the Dice score distributions, violin plots for the

Table 3: Mean Dice similarity scores for various classes in the PENGWIN dataset. The highest scores are emphasised in **bold**, and the second-highest are underlined. Unit: %.

Methods	Left hipbone	Right hipbone	Sacrum	Background	Average
UNet++ (Zhou et al., 2019)	70.92	70.77	<b>92.56</b>	<b>99.87</b>	83.53
SegMamba (Xing et al., 2024)	86.56	86.56	<u>90.57</u>	<u>99.86</u>	90.89
3DUX-Net (Lee et al., 2023)	66.13	63.37	86.77	99.80	79.02
SwinUNETR-V2 (He et al., 2023)	85.99	86.14	86.44	99.82	89.60
nnUNet (Isensee et al., 2021)	<u>90.74</u>	<u>91.22</u>	90.38	<u>99.86</u>	<b>93.05</b>
TransUNet (Chen et al., 2024)	70.40	70.57	85.00	99.77	81.43
UNetR++ (Shaker et al., 2024)	86.91	86.98	84.43	99.79	89.53
<b>MobileViM<sub>s</sub> (ours)</b>	<b>92.15</b>	<b>92.18</b>	86.76	99.81	<u>92.72</u>
<b>MobileViM<sub>xs</sub> (ours)</b>	87.27	87.16	85.67	99.78	89.97

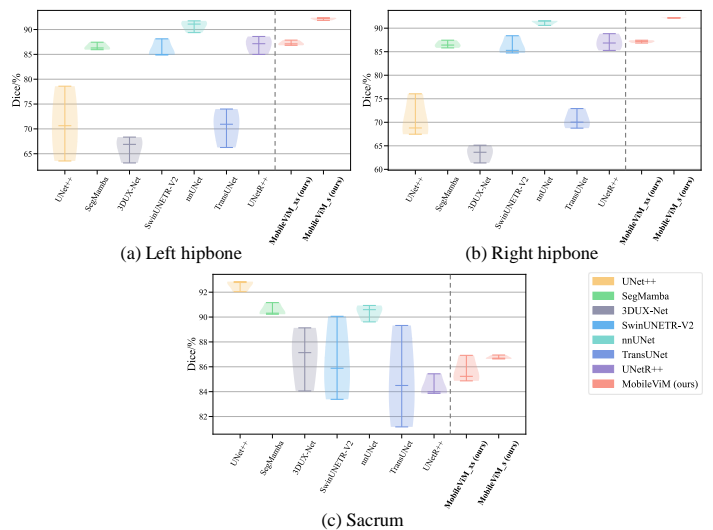


Fig. 6: Distribution of segmentation Dice similarity scores for left hipbone, right hipbone, and sacrum in the PENGWIN dataset.

first three classes — left hipbone, right hipbone, and sacrum — are created and presented in Fig. 6. While UNet++ showed a tight clustering around the highest median in the sacrum class, it exhibited a wider spread with comparatively low medians in the left and right hipbone classes, suggesting imbalanced performance and instability across three classes. The relatively broad bases of the violin plots for 3DUX-Net, SwinUNETR-V2, and TransUNet, as indicated in Fig. 6, suggest a high variation of segmentation performance. Such variations denote that these models may not consistently deliver accurate segmentations. In contrast, the narrower shapes of the violin plots for MobileViMs compared to baseline models signify a more consistent range of segmentation Dice scores. As depicted in Fig. 6ab, MobileViMs demonstrated significantly high median values across left and right hipbone classes, suggesting robust performance in identifying pelvic fractures.

In summary, the data presented in Tabs. 2 and 3 and Figs. 5 and 6 confirm that MobileViMs are not only efficient in terms of parameter count and computational demands, achieving rapid inference speeds, but also demonstrate accurate and reliable differentiation capabilities for clinical diagnostics using 3D imag-

Table 4: Ablation study results for key components of MobileViM\_s. The best outcomes are highlighted in **bold**.

Ablation settings				Computational efficiency		PENGWIN		ATLAS	
Scale bridger	Mamba module	Dimensional independence	Dual direction	# Params /million	Speed /FPS	Dice/%	p-value	Dice/%	p-value
				<b>0.48</b>	<b>548</b>	39.39	-	66.05	-
✓				5.46	140	67.16	$2 \times 10^{-6}$	73.37	$6 \times 10^{-6}$
✓	✓			17.81	35	75.53	$1 \times 10^{-6}$	75.53	$1 \times 10^{-6}$
✓	✓	✓		6.27	111	83.86	$1 \times 10^{-6}$	78.15	$1 \times 10^{-6}$
✓	✓		✓	17.87	21	79.95	$1 \times 10^{-6}$	76.55	$1 \times 10^{-6}$
	✓	✓	✓	1.06	104	50.60	$2 \times 10^{-6}$	68.67	$4 \times 10^{-4}$
✓	✓	✓	✓	6.29	91	<b>92.72</b>	$1 \times 10^{-6}$	<b>80.60</b>	$1 \times 10^{-6}$

ing technologies such as CT and MRI. These attributes make MobileViMs highly suitable for real-time clinical applications, contrasting sharply with other models despite their larger sizes and computational loads, demonstrating significantly slower processing speeds.

#### 4.3. Ablation Studies

All ablation studies were carried out using the PENGWIN and ATLAS datasets. This section details the effect of each key component within the architecture of MobileViM\_s (*i.e.*, scale bridger, vision Mamba, dimension-independent mechanism, and dual-direction traversing approach) on performance.

The data from the first and second rows of Tab. 4 show that the addition of the scale bridger module led to Dice score improvements of +27.77% and +7.32% in the PENGWIN and ATLAS datasets, respectively. Furthermore, integrating the vanilla Mamba module resulted in additional Dice score increases of +8.37% and +2.16% beyond what the vanilla scale bridger achieved for detecting resection pelvic fractures and liver tumours, respectively. Incorporating the dimension-independent mechanism into the Mamba module further improved its performance, with enhancements of +8.33% and +2.62% Dice scores for the PENGWIN and ATLAS datasets, respectively. Additionally, adopting dual-direction scanning within the Mamba module led to further improvements of 4.42% and 1.02% in Dice scores for the same datasets. By combining the dimension-independent mechanism and dual-direction approach within the vanilla Mamba module, Dice scores increased to 92.72% and 80.60% in the PENGWIN and ATLAS datasets, respectively. These results demonstrate that these modules significantly enhance the diagnostic capabilities of 3D medical imaging.

Further analysis from Tab. 4 reveals the scale bridger outperformed the enhancements provided by the Mamba module with both the dimension-independent mechanism and the dual-direction traversing (fully-equipped Mamba module), achieving improvements of +16.56% and +4.70%. However, while integrating the scale bridger led to significantly faster inference speeds of 140 FPS, it also resulted in a larger model size, with a parameter count of 5.46 million compared to 1.06 million parameters and 104 FPS when incorporating only the fully-equipped Mamba module. When the scale bridger and the fully-equipped Mamba module are combined, MobileViM\_s operates at a reduced speed of 91 FPS with a higher parameter

count of 6.29 million. Despite this, the combination of all proposed modules in MobileViM\_s delivers the most favourable outcomes in terms of both performance and computational efficiency. The statistical significance of these improvements is underscored by all p-values for Dice scores being below 0.001, which confirms the results' reliability.

#### 4.4. Negative Case Analysis

To evaluate segmentation quality and conduct error analysis, we present visual examples of segmentation results from various models across datasets, including PENGWIN, BraTS2024, ATLAS, and ToothFairy2, as illustrated in Fig. 7. To clarify the comparisons, the largest versions of MobileViM were chosen.

In Fig. 7a, models from the control group failed to accurately outline the complete boundaries of the sacrum, left hipbone, and right hipbone. Notably, UNet++, SegMamba, 3DUX-Net, SwinUNetR-V2, and nnUNet incorrectly identified large cavities within the left and right hipbones, whereas the ground truth indicates a smaller cavity only within the right hipbone and none in the left. Additionally, TransUNet failed to distinguish between the left and right hipbones, as evidenced by noticeable colour gradients in their segmentation outputs. Furthermore, UNetR++ incorrectly classified the left hipbone as the right hipbone and missed segmenting the right hipbone. All methods in the control group also represented the sacrum as smaller than indicated by the ground truth. Conversely, MobileViM\_s accurately segmented these three anatomical regions, closely aligning with the ground truth annotations. Although MobileViM\_s did not capture the hollow in the right hipbone, it accurately identified cavities in the sacrum.

For brain cancer diagnosis, as shown in the Fig. 7b, all methods inaccurately identified a gross tumour volume near the forehead, diverging from the actual location of the tumour as represented by the ground truth. However, MobileViM\_s pinpointed the correct tumour location and precisely delineated the tumour boundaries. In the context of liver tumour detection, Fig. 7c shows that all control group methods failed to detect tumour regions within the liver and struggled with accurately identifying internal structures. Specifically, UNet++, 3DUX-Net, SwinUNetR-V2, nnUNet, and UNetR++ treated multiple separate tumour regions as a single entity. Conversely, SegMamba and TransUNet either missed two tumour regions or underestimated the sizes of the tumours. In stark contrast, MobileViM\_s

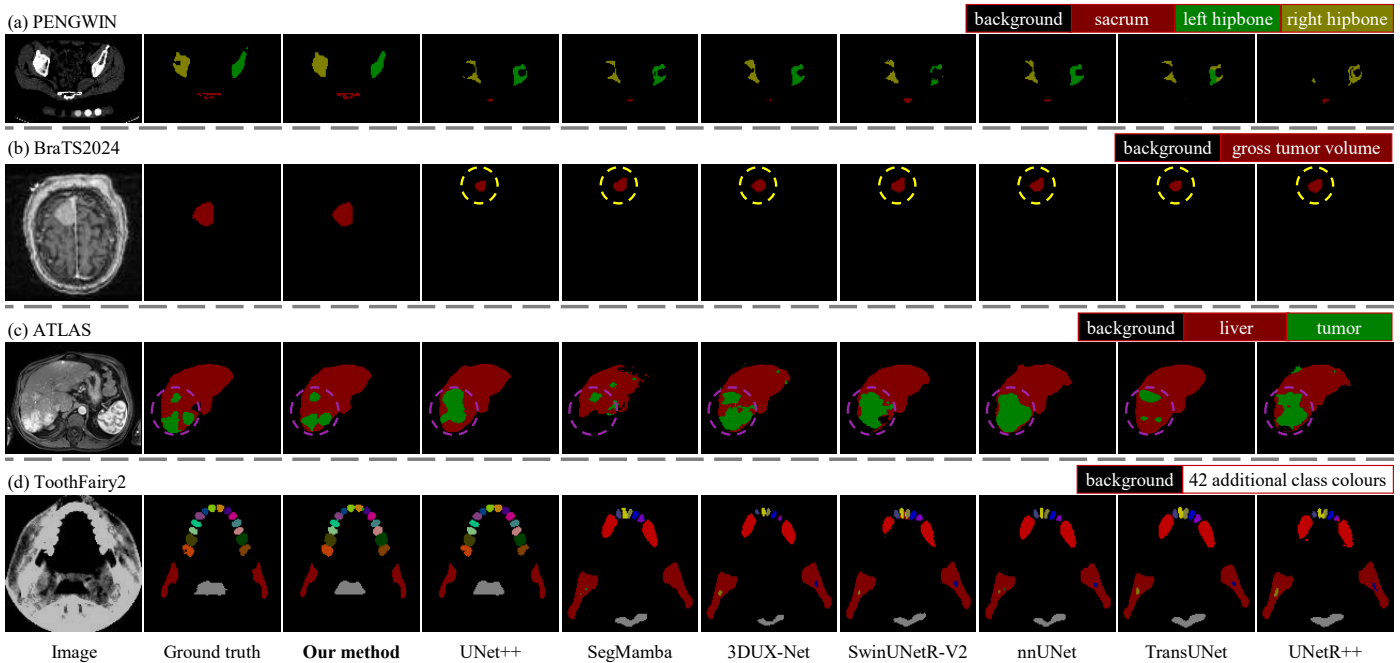


Fig. 7: Qualitative visualisation of segmentation results of the proposed method and baseline approaches on (a) PENGWIN, (b) BraTS2024, (c) ATLAS, and (d) ToothFairy2 datasets.

successfully discovered the three regions of liver tumours and significantly replicated their sizes compared to the ground truth.

Regarding the diagnosis of dental structures, as depicted in the Fig. 7d, only MobileViM<sub>s</sub> and UNet++ correctly identified the types and shapes of teeth. Other models failed to recognise posterior teeth and could not accurately differentiate among anterior teeth in the lower jaw. Furthermore, except for MobileViM<sub>s</sub> and UNet++, the other tested methods inaccurately depicted larger lower jaw bones than those shown in the ground truth. Additionally, these methods incorrectly located the pharynx, potentially increasing the risk of medical complications during surgeries.

These visual results, consistent with the discussions in Sec. 4.2, highlight MobileViM's substantial capability for application across various medical imaging modalities, offering significant advantages in disease diagnostics and surgical planning.

## 5. Discussion

With the introduction of two scales of MobileViM, these models can be adapted to a wide range of application scenarios. For instances where high diagnosis performance is critical, MobileViM<sub>s</sub> is recommended. Operating with 6.29 million parameters and achieving 91 FPS on an NVIDIA RTX 4090, MobileViM<sub>s</sub> meets high-performance requirements while maintaining relatively low computation demands. For environments with less powerful hardware, such as lower-end GPUs, laptops, smartphones, and cost-effective microcontrollers, MobileViM<sub>xs</sub> becomes a viable option.

The dimension-independent (Dimin) mechanism, which requires comparatively low parameters, holds significant promise for real-time medical imaging applications. These modules can

be crucial in expanding the scope of medical technology applications. Furthermore, the Dimin mechanism provides a new approach for handling multidimensional data through patch representation learning. Whether dealing with 2D, 3D or higher-dimensional data, the Dimin mechanism processes it along a single dimension, which reduces computational demands and enhances diagnostic performance.

Recent advancements in foundation vision models have demonstrated impressive results across various medical imaging tasks (Ma *et al.*, 2024). These models primarily utilise CNNs or ViTs. The MobileViM framework offers fresh perspectives on designing foundation models based on the Mamba architecture. Additionally, the light-weight techniques proposed in this work could inspire the foundation model community to develop models more applicable to mobile deployment.

## 6. Conclusion

This paper introduces MobileViMs, the mobile networks that integrate the Mamba model with the dimension-independent mechanism and dual-direction traversing technique and the scale bridger framework to efficiently analyse 3D medical images, aiding in the detection of life-threatening diseases. The experimental results demonstrate that MobileViMs are highly effective in processing various medical imaging modalities. MobileViMs outperformed other SOTA methods, achieving a decrease in parameters count up to -106.45 million and increases in Dice scores up to 9.79% and 3.66% across the BraTS2024 and ATLAS datasets, respectively, at over 90 FPS. MobileViM<sub>s</sub> also achieved the second-highest Dice similarity scores of 92.72% and 77.43% in the PENGWIN and Toothfairy2 datasets. The visualisation results further confirm that MobileViMs can accurately identify regions of interest in 3D medical

images, demonstrating their exceptional capability in medical image segmentation. These findings highlight the potential of MobileViMs as a significant advancement in 3D medical image analysis.

## References

- Anonymous, 2024. Q-Mamba: Towards more efficient mamba models via post-training quantization, in: Submitted to The Thirteenth International Conference on Learning Representations.
- Chen, J., Mei, J., Li, X., Lu, Y., Yu, Q., Wei, Q., Luo, X., Xie, Y., Adeli, E., Wang, Y., et al., 2024. TransUNet: Rethinking the u-net architecture design for medical image segmentation through the lens of transformers. *Medical Image Analysis* 97, 103280.
- Chen, L.C., Papandreou, G., Kokkinos, I., Murphy, K., Yuille, A.L., 2017. DeepLab: Semantic image segmentation with deep convolutional nets, atrous convolution, and fully connected crfs. *IEEE Transactions on Pattern Analysis and Machine Intelligence* 40, 834–848.
- Dai, W., Liu, R., Wu, T., Wang, M., Yin, J., Liu, J., 2024a. Deeply supervised skin lesions diagnosis with stage and branch attention. *IEEE Journal of Biomedical and Health Informatics* 28, 719–729.
- Dai, W., Liu, R., Wu, Z., Wu, T., Wang, M., Zhou, J., Yuan, Y., Liu, J., 2024b. Exploiting scale-variant attention for segmenting small medical objects. *arXiv:2407.07720*.
- Dai, W., Wu, Z., Liu, R., Wu, T., Wang, M., Zhou, J., Zhang, Z., Liu, J., 2024c. Automated non-invasive analysis of motile sperms using sperm feature-correlated network. *IEEE Transactions on Automation Science and Engineering*.
- Dai, W., Wu, Z., Liu, R., Zhou, J., Wang, M., Wu, T., Liu, J., 2024d. SoSegFormer: A cross-scale feature correlated network for small medical object segmentation, in: 2024 IEEE International Symposium on Biomedical Imaging (ISBI), IEEE. pp. 1–4.
- Dao, T., Gu, A., 2024. Transformers are SSMS: Generalized models and efficient algorithms through structured state space duality, in: International Conference on Machine Learning.
- Gu, A., Dao, T., 2024. Mamba: Linear-time sequence modeling with selective state spaces, in: First Conference on Language Modeling.
- Gu, A., Goel, K., Re, C., 2022. Efficiently modeling long sequences with structured state spaces, in: International Conference on Learning Representations.
- He, Y., Nath, V., Yang, D., Tang, Y., Myronenko, A., Xu, D., 2023. SwinUNETR-V2: Stronger swin transformers with stagewise convolutions for 3d medical image segmentation, in: International Conference on Medical Image Computing and Computer-Assisted Intervention, Springer. pp. 416–426.
- Hou, Q., Zhou, D., Feng, J., 2021. Coordinate attention for efficient mobile network design, in: Proceedings of the IEEE/CVF Conference on Computer Vision and Pattern Recognition, pp. 13713–13722.
- Howard, A., Sandler, M., Chu, G., Chen, L.C., Chen, B., Tan, M., Wang, W., Zhu, Y., Pang, R., Vasudevan, V., et al., 2019. Searching for MobileNetV3, in: Proceedings of the IEEE/CVF international conference on computer vision, pp. 1314–1324.
- Hwang, S., Lahoti, A., Puduppully, R., Dao, T., Gu, A., 2024. Hydra: Bidirectional state space models through generalized matrix mixers, in: The Thirty-eighth Annual Conference on Neural Information Processing Systems, Neural Information Processing Systems. pp. 1–33.
- Isensee, F., Jaeger, P.F., Kohl, S.A., Petersen, J., Maier-Hein, K.H., 2021. nnUNet: A self-configuring method for deep learning-based biomedical image segmentation. *Nature Methods* 18, 203–211.
- LaBella, D., Schumacher, K., Mix, M., Leu, K., McBurney-Lin, S., Nedelec, P., Villanueva-Meyer, J., Shapey, J., Vercauteren, T., Chia, K., et al., 2024. Brain tumor segmentation (BraTS) challenge 2024: Meningioma radiotherapy planning automated segmentation. *arXiv preprint arXiv:2405.18383*.
- Lee, H.H., Bao, S., Huo, Y., Landman, B.A., 2023. 3D UX-Net: A large kernel volumetric convnet modernizing hierarchical transformer for medical image segmentation, in: The Eleventh International Conference on Learning Representations.
- Lee, S., Choi, J., Kim, H.J., 2024. EfficientViM: Efficient vision mamba with hidden state mixer based state space duality. *arXiv preprint arXiv:2411.15241*.
- Liu, J., Yang, H., Zhou, H.Y., Xi, Y., Yu, L., Li, C., Liang, Y., Shi, G., Yu, Y., Zhang, S., et al., 2024a. Swin-UMamba: Mamba-based unet with imagenet-based pretraining, in: International Conference on Medical Image Computing and Computer-Assisted Intervention, Springer. pp. 615–625.
- Liu, R., Zhu, Y., Wu, C., Guo, H., Dai, W., Wu, T., Wang, M., Li, W.J., Liu, J., 2023a. Interactive dual network with adaptive density map for automatic cell counting. *IEEE Transactions on Automation Science and Engineering*.
- Liu, Y., Tian, Y., Zhao, Y., Yu, H., Xie, L., Wang, Y., Ye, Q., Jiao, J., Liu, Y., 2024b. VMamba: Visual state space model. *arXiv:2401.10166*.
- Liu, Y., Yibulayimu, S., Sang, Y., Zhu, G., Wang, Y., Zhao, C., Wu, X., 2023b. Pelvic fracture segmentation using a multi-scale distance-weighted neural network, in: International Conference on Medical Image Computing and Computer-Assisted Intervention, Springer. pp. 312–321.
- Long, J., Shelhamer, E., Darrell, T., 2015. Fully convolutional networks for semantic segmentation, in: Proceedings of the IEEE Conference on Computer Vision and Pattern Recognition, pp. 3431–3440.
- Loshchilov, I., Hutter, F., 2017. Decoupled weight decay regularization. *arXiv preprint:1711.05101*.
- Loshchilov, Ilya and Hutter, Frank, 2016. SGDR: Stochastic gradient descent with warm restarts, in: International Conference on Learning Representations, pp. 1–16.
- Lumetti, L., Pipoli, V., Bolelli, F., Ficarra, E., Grana, C., 2024. Enhancing patch-based learning for the segmentation of the mandibular canal. *IEEE Access*.
- Ma, J., He, Y., Li, F., Han, L., You, C., Wang, B., 2024. Segment anything in medical images. *Nature Communications* 15, 654.
- Mehta, S., Rastegari, M., 2021. MobileViT: Light-weight, general-purpose, and mobile-friendly vision transformer, in: International Conference on Learning Representations.
- Milletari, F., Navab, N., Ahmadi, A., 2016. V-Net: Fully convolutional neural networks for volumetric medical image segmentation, in: IEEE International Conference on 3D Vision (arXiv: 1606.04797).
- Paszke, A., Gross, S., Massa, F., Lerer, A., Bradbury, J., Chanan, G., Killeen, T., Lin, Z., Gimelshein, N., Antiga, L., et al., 2019. PyTorch: An imperative style, high-performance deep learning library. *Advances in Neural Information Processing Systems* 32, 1–12.
- Pei, X., Huang, T., Xu, C., 2024. EfficientVMamba: Atrous selective scan for light weight visual mamba. *arXiv preprint arXiv:2403.09977*.
- Quinton, F., Popoff, R., Presles, B., Leclerc, S., Meriaudeau, F., Nodari, G., Lopez, O., Pellegrinelli, J., Chevallier, O., Ginhad, D., et al., 2023. A tumour and liver automatic segmentation (ATLAS) dataset on contrast-enhanced magnetic resonance imaging for hepatocellular carcinoma. *Data* 8, 79.
- Ronneberger, O., Fischer, P., Brox, T., 2015. U-Net: Convolutional networks for biomedical image segmentation, in: International Conference on Medical Image Computing and Computer Assisted Intervention, Springer. pp. 234–241.
- Ruan, J., Xiang, S., 2024. VM-UNet: Vision Mamba unet for medical image segmentation. *arXiv preprint arXiv:2402.02491*.
- Shaker, A.M., Maaz, M., Rasheed, H., Khan, S., Yang, M.H., Khan, F.S., 2024. UNETR++: Delving into efficient and accurate 3d medical image segmentation. *IEEE Transactions on Medical Imaging*.
- Vasu, P.K.A., Gabriel, J., Zhu, J., Tuzel, O., Ranjan, A., 2023. MobileOne: An improved one millisecond mobile backbone, in: Proceedings of the IEEE/CVF conference on computer vision and pattern recognition, pp. 7907–7917.
- Xing, Z., Ye, T., Yang, Y., Liu, G., Zhu, L., 2024. SegMamba: Long-range sequential modeling mamba for 3d medical image segmentation, in: International Conference on Medical Image Computing and Computer-Assisted Intervention, Springer. pp. 578–588.
- Yao, J., Hong, D., Li, C., Chanussot, J., 2024. SpectralMamba: Efficient mamba for hyperspectral image classification. *arXiv preprint arXiv:2404.08489*.
- Zhang, R., Chung, A.C., 2024. EfficientQ: An efficient and accurate post-training neural network quantization method for medical image segmentation. *Medical Image Analysis* 97, 103277.
- Zhou, Z., Siddiquee, M.M.R., Tajbakhsh, N., Liang, J., 2019. UNet++: Redesigning skip connections to exploit multiscale features in image segmentation. *IEEE Transactions on Medical Imaging* 39, 1856–1867.
- Zhu, L., Liao, B., Zhang, Q., Wang, X., Liu, W., Wang, X., 2024. Vision Mamba: Efficient visual representation learning with bidirectional state space model, in: International Conference on Machine Learning.
- Zhu, Y., Zhang, D., Lin, Y., Feng, Y., Tang, J., 2025. Merging context clustering with visual state space models for medical image segmentation. *IEEE Transactions on Medical Imaging*.